

# Elastic softening and defect-mediated diffusion in superionic $\text{Li}_2\text{O}$ revealed by molecular dynamics

Zhifeng Wu , Yawei You , Fangfang Zhang , Tie-Yu Lü , Xinrui Cao , Yang Sun , Zi-Zhong Zhu , and Shunqing Wu \*

*Department of Physics, OSED, Key Laboratory of Low Dimensional Condensed Matter Physics (Department of Education of Fujian Province), Xiamen University, Xiamen 361005, China*



(Received 27 June 2025; revised 30 August 2025; accepted 16 October 2025; published 12 November 2025)

The superionic transition in lithium oxide ( $\text{Li}_2\text{O}$ ) presents significant challenges in establishing the structure-property relationship between its microscopic dynamical behavior to macroscopic physical properties. Additionally, the fundamental mechanism driving this transition remains contentious due to competing theoretical interpretations. Using machine learning potentials that maintain *ab initio*-level precision while enabling extended in both temporal and spatial scales, we systematically investigate lithium-ion diffusion dynamics spanning from crystalline to superionic phases. Our results give a clear physical pattern of  $\text{Li}_2\text{O}$  Arrhenius plot throughout three distinct regions. The elastic softening serves as a signal of accelerating of Li-ions movement. Superionic transition is manifested in the melting of the Li sublattice. Dynamical analysis indicates that the superionic transition is driven by the formation of Frenkel pairs. Octahedral interstitial Li-ions, increasing sharply near the superionic state, act as primary diffusion carriers. The tetrahedral Li-ions exhibit much lower individual mobility and play a secondary role in diffusion under superionic state. This highlights the unique defect-mediated nature of diffusion in superionic state.

DOI: [10.1103/4z6n-zfdr](https://doi.org/10.1103/4z6n-zfdr)

## I. INTRODUCTION

The deuterium(D)-tritium(T) nuclear fusion reaction stands as a pivotal candidate for addressing global energy sustainability, with tritium breeding blanket materials serving as critical components for fuel regeneration in fusion reactors [1,2]. Among lithium-containing ceramics—including  $\text{Li}_2\text{O}$ ,  $\text{Li}_2\text{TiO}_3$ ,  $\text{LiAlO}_2$ , and  $\text{Li}_2\text{ZrO}_3$  [1,2]— $\text{Li}_2\text{O}$  emerges as a prime candidate due to its exceptional combination of high melting point and high ionic conductivity at specific temperature, and low  $\text{LiOH}$  solubility [3]. Crucially, the tritium release kinetics in  $\text{Li}_2\text{O}$ -dominated systems are governed by lithium vacancy ( $V_{\text{Li}}$ ) diffusion barriers [3], making atomic-scale understanding of  $\text{Li}^+$  transport mechanisms imperative for both material design and reactor operation.

Similar to various fluorite or antifluorite structured compounds, such as  $\text{UO}_2$  [4,5],  $\text{Li}_2\text{S}$  [6], and  $\text{CaF}_2$  [7],  $\text{Li}_2\text{O}$  undergoes a superionic transition at elevated temperature. There exists two types of superionic transition [8]. Type I superionic transition occurs with a sudden change of diffusion coefficient (as seen in  $\text{CuI}$  [9],  $\alpha\text{-KAg}_3\text{Se}_2$  [10]) accompanied by a distinct phase transition, during which some types of ions rearrange while others exhibit fast ionic diffusion. Type II superionic transition occurs without any rearrangement, and is associated with a second-order phase transition, as found in  $\text{Li}_3\text{N}$  [11],  $\text{Li}_3\text{YCl}_6$  [12], and  $\text{H}_2\text{O}$  [13]. In the superionic state, materials exhibit properties intermediate between liquid and solid, such as liquidlike ionic diffusion behavior in a stable solid framework. These characteristics make superionic materials highly promising for applications in solid-state electrolyte [14–16] and solid oxide fuel cells [17,18].

The distinctive properties of  $\text{Li}_2\text{O}$  have been well investigated through both experiment and computational approaches. Notably,  $\text{Li}_2\text{O}$  has been reported to undergo a superionic transition at temperatures ranging from  $\sim 1200$  K (as reported in inelastic neutron experiments [19,20]) to 1400–1600 K (as predicted by molecular dynamics (MD) simulations [21]), and with *ab initio* molecular dynamics (AIMD) simulation suggesting a transition threshold above 1300 K [22]. Nuclear magnetic resonance (NMR) has been employed to probe  $\text{Li}_2\text{O}$  self-diffusion at specific temperature [2]. Concurrently, lattice dynamics study revealed rapid Li-ion diffusion at 1000 K [23]. MD simulations have further characterized the role of defects in  $\text{Li}_2\text{O}$  by quantifying their influence on the diffusion coefficient [24]. More recently, a cluster expansion method combined with kinetic Monte Carlo has extended  $\text{Li}_2\text{O}$  Arrhenius plot to room temperature [25].

Despite extensive research on  $\text{Li}_2\text{O}$ , notable gaps remain. The structure-property relationship between its microscopic dynamic behavior and macroscopic physical properties, such as ionic conductivity and elastic modulus, remains unclear. Additionally, the microscopic mechanism underlying the superionic transition is poorly understood and continues to be a topic of debate, hindering a deeper understanding of this phenomenon. In the meanwhile, the existing methodologies exhibit significant limitations. Density functional theory (DFT) method only supports small models, leading to a finite-size effect [26–30]. Conventional MD simulation, often relying on empirical potentials, are difficult to accurately capture the dynamical behavior across wide temperature ranges. To address these challenges, machine learning potentials (MLPs) have emerged as a transformative solution, offering DFT-level accuracy while enabling access to larger systems and longer simulation timescales [31–37].

\*Contact author: wsq@xmu.edu.cn

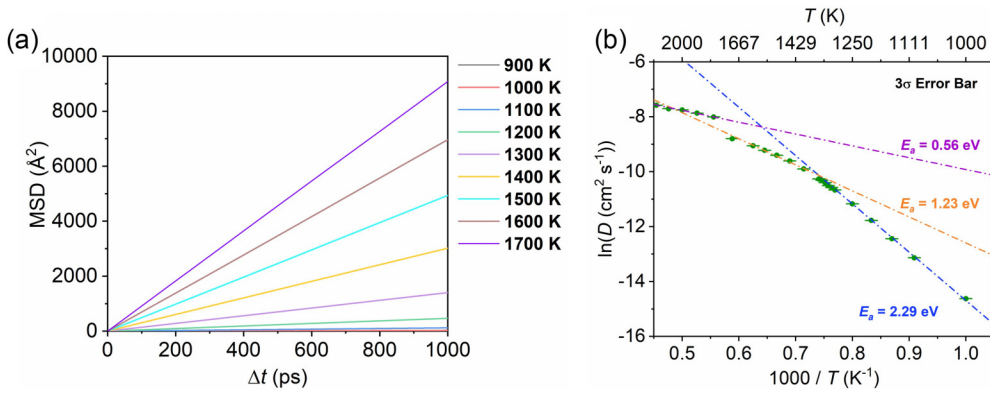


FIG. 1.  $\text{Li}_2\text{O}$  diffusion behavior. (a) The calculated time-averaged mean square displacement of  $\text{Li}^+$ -ions in  $\text{Li}_2\text{O}$ . (b)  $\text{Li}^+$ -ions diffusion coefficients. The color lines exhibit exponential fits at different regions. Error bars are within the symbol size.

In this work, we combine deep potential [36,38] with MD simulations to comprehensively investigate the dynamical characteristics of  $\text{Li}_2\text{O}$ , with a focus on its superionic transition. This approach allows for the precise quantification of atomic-level behavior across a wide temperature range. Most notably, our work highlights the distinct dynamical regimes across a wide temperature range, the understanding of the structure-property relationship between dynamical characteristics and macroscopic physical properties, and uncovers the key mechanisms driving fast-ion diffusion in the superionic state. These insights provide critical guidelines for designing  $\text{Li}_2\text{O}$ -based materials for energy storage and conversion applications.

## II. METHODS

Our machine learning dataset was constructed by first-principles calculations. The first-principles calculations were conducted by Vienna *ab initio* simulation package (VASP) [39,40]. The calculations employed the projected augmented wave (PAW) method [41] with the Perdew-Burke-Ernzerhof (PBE) [42] generalized gradient approximation (GGA) for the exchange-correlation functional. A plane-wave cutoff energy of 520 eV was adopted, and Brillouin-zone sampling was conducted using a  $\Gamma$ -centered Monkhorst-Pack  $k$ -point grid with a spacing of  $0.3 \text{ \AA}^{-1}$  for structure optimization.

The deep potential model was trained using the DeePMD-kit package [38] and deployed for molecular dynamics simulations via used deep potential molecular dynamics (DPMD) framework [36]. The model incorporated a cutoff radius of  $6.0 \text{ \AA}$  with a smoothing width of  $0.5 \text{ \AA}$  to capture local atomic environments. The neural network architecture consisted of an embedding net with three hidden layers [10,20,40] and a fitting net of [120, 120, 120]. Training was performed for 6 000 000 steps using the Adam stochastic gradient descent method [43], leading to an exponential decrease in the learning rate starting from 0.001. The energy prefactor was scaled from 0.02 to 2, while the virial and force prefactors were annealed from 1000 to 1 during training. This model was initialized from our pretrained deep potential model [44,45], with training strategies and dataset selection detailed in Note 1 in the Supplemental Material [46].

Other calculation methods can be seen in Note 2 in the Supplemental Material [46]. The reliability of the deep potential function can be seen in Note 3 in the Supplemental Material [46].

## III. RESULTS AND DISCUSSION

### A. Ionic diffusion

The time-averaged mean square displacement (MSD) of  $\text{Li}^+$  ions is presented in Fig. 1(a). At 900 K (see Fig. S7 [46]), the MSD reaches only  $4.0 \text{ \AA}^2$  after 1 ns of simulation, which is smaller than both the squared nearest-neighbor  $\text{Li}^+ - \text{Li}^+$  distance ( $\sim 5.4 \text{ \AA}^2$ ) and the  $\text{Li}^+$ -to-nearest-octahedral-interstitial distance ( $\sim 3.9 \text{ \AA}^2$ ), where subdiffusive behavior is observed. This confinement indicates that  $\text{Li}^+$  vibrations dominate below  $\sim 900$  K, with few diffusion events (termed “MSD limitation” [47]). Consequently, calculating diffusion coefficients from the MSD slope is invalid in this regime. Notably, the MSD exhibits linearity at all temperatures except 900 K.

The temperature dependence of the diffusion coefficient is shown in the Arrhenius plot [Fig. 1(b)]. Linear fitting identifies three distinct regions in  $\text{Li}_2\text{O}$ : the normal state (activation energy  $E_a = 2.29 \text{ eV}$ ), the fast ion region—superionic state ( $E_a = 1.23 \text{ eV}$ , onset at  $\sim 1300$  K)—and the liquid phase region ( $E_a = 0.56 \text{ eV}$ , transition at  $\sim 1700$  K). This behavior aligns with superionic materials like  $\text{UO}_2$  [5,48],  $\text{Li}_3\text{N}$  [11], and  $\text{Li}_3\text{YCl}_6$  [12]. The decrease in  $E_a$  at 1300 K signals the superionic transition, while the discontinuity at  $\sim 1700$  K corresponds to melting of  $\text{Li}_2\text{O}$ . In liquid region, the reduced activation energy facilitates a faster  $\text{Li}^+$ -ions diffusion. Besides, it's worth noting that the calculated ionic conductivity exceeds 1 S/cm above 1300 K (Fig. S8 [46]), further confirming the superionic transition in  $\text{Li}_2\text{O}$ , consistent with prior reports [8].

The Arrhenius behavior of lithium oxide has been widely studied. While Gupta [19] reported a detailed analysis of Li-ion diffusion, the assumption of constant activation energy across all temperatures remains debated. Oishi *et al.* [49] divided the Arrhenius plot into two regions: a low-temperature regime ( $E_a = 23.4 \times 10^3 \text{ kcal/mol}$ ) and a high-temperature region ( $E_a = 58.2 \times 10^3 \text{ kcal/mol}$ ) as shown in Fig. S9 [46]. However, this abrupt increase in activation energy contradicts

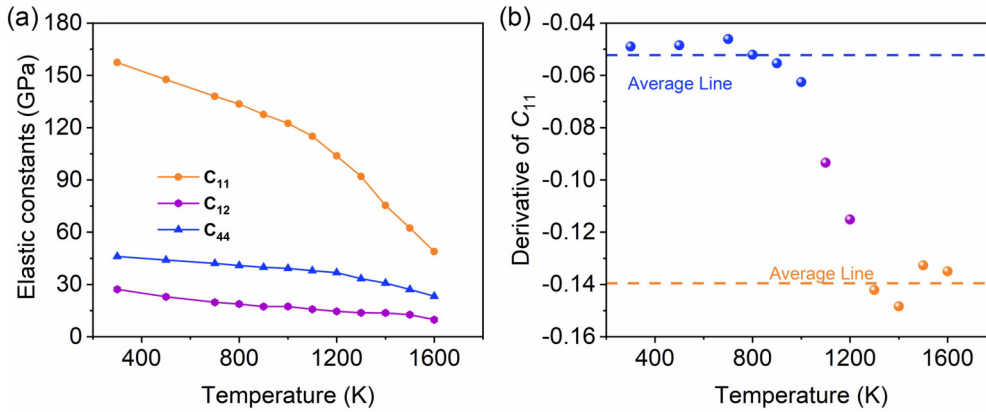


FIG. 2.  $\text{Li}_2\text{O}$  Elastic properties. (a) Elastic constants of  $\text{Li}_2\text{O}$ . (b) The temperature derivative of  $C_{11}$  in (a). The horizontal dashed lines represent the average derivative in the range of 300–1000 K and 1300–1600 K, respectively.

the typical decrease expected during superionic transitions. Lörger *et al.* [50] reported an Arrhenius profile distinct from ours, likely due to their use of cation doping—an extrinsic vacancy source—contrasted with our focus on thermally induced intrinsic defects. Our results align with [47] but exhibit higher precision, revealing that the Arrhenius slope magnitude is smaller in the superionic state and larger in the normal state, directly correlated with the activation energies of the respective states. Importantly, we confirm that lithium oxide followed Arrhenius kinetics across three distinct temperature intervals, with each interval characterized by unique activation energies. The activation energy extracted from the Arrhenius plot represents an effective average over all possible Li-ions migration events, rather than the barrier of a single path. Detailed migration barriers along specific crystallographic directions have been reported in previous studies [51,52].

### B. Elastic constants and dynamics behavior

Elastic constants are key indicators of superionic transition. In  $\text{Li}_2\text{O}$ , high temperature  $C_{11}$  softening has been identified as a signature of superionic behavior [5,13,20,22,53,54]. Figure 2(a) shows our calculated elastic constants. While  $C_{12}$  and  $C_{44}$  decrease smoothly and linearly across all temperatures,  $C_{11}$  exhibits two distinct regions. Below 1000 K,  $C_{11}$  decreased linearly; between 1100–1200 K, pronounced softening occurs; above 1300 K, it resumes decreases linearly but with a shallower slope. The temperature derivative of  $C_{11}$ , as shown in Fig. 2(b), highlights these regions via dashed lines denoting average slopes for 300–1000 K and 1300–1600 K.

The O sublattice remains rigid up to 1700 K, as evidenced by the vibration-dominated O MSD and negligible diffusion at 1700 K (Fig. S6 [46]), isolating Li-ion dynamics as the origin of elastic softening. To correlate with Li mobility, Figs. 3(a)–3(c) show atomic trajectories: at 900 K, Li ions are mostly localized; by 1100 K, enhanced diffusion coincides with  $C_{11}$  softening; and at 1300 K, Li delocalization and sublattice melting confirm a type II superionic transition, with Li-ions diffusing through O octahedral sites. By 1800 K, the distribution of Li and O is shown in Fig. 3(d), where the entire system completes melting into the liquid phase.

The van Hove self-correlation function can be used to observe vibration and diffusion behavior. It is defined as follows:

$$G_s(\mathbf{r}, \Delta t) = \frac{1}{N} \left\langle \sum_i^N \delta(\mathbf{r} + \mathbf{r}_i(0) - \mathbf{r}_i(\Delta t)) \right\rangle. \quad (1)$$

$N$  is the calculated atom number.  $\Delta t$  is a period of time, which should be selective containing a complete diffusion

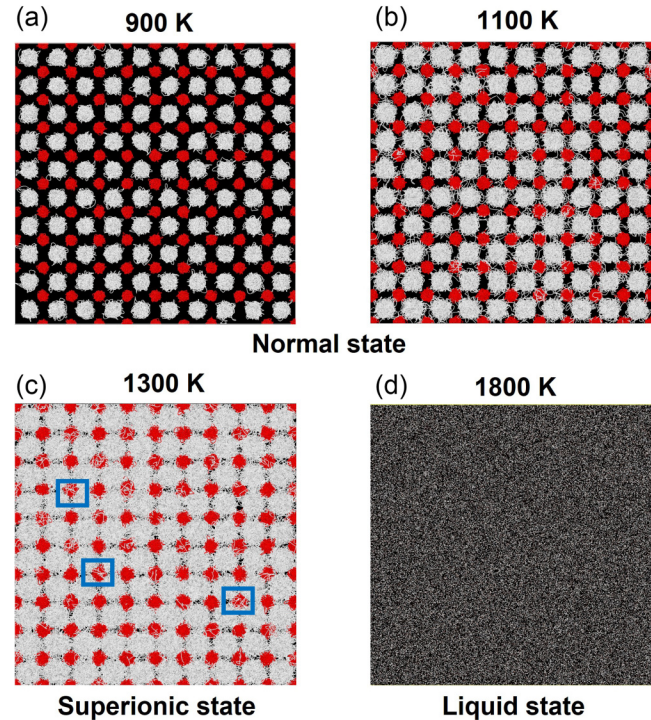


FIG. 3.  $\text{Li}_2\text{O}$  diffusion behaviors. (a)–(c) Trajectories of Li (white) and O (red) during 20 ps at 900 K, 1100 K, and 1300 K, respectively. The blue boxes in (c) highlight the typical phenomenon where Li occupied the octahedral interstitial positions during the diffusion process. (d) Distribution of Li (white) and O (red) at 1800 K. To better reveal the characteristics of the melted state, multiple frames were superimposed and the atoms were plotted with small sizes.

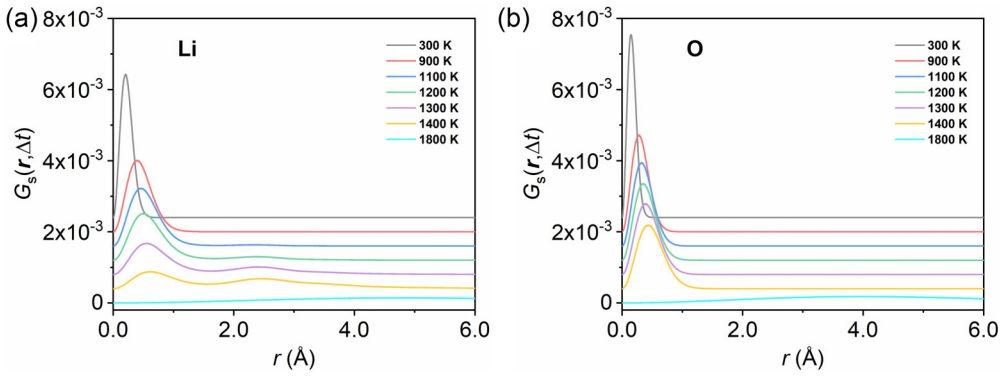


FIG. 4. The van Hove self-correlation function of Li (a) and O (b).  $\Delta t$  was set to be 2 ps. All curves were vertically shifted for clarity and ease of comparison.

or vibration event.  $r_i(0)$  is atom's initial position.  $r_i(\Delta t)$  is atom's position at  $t = \Delta t$ , which is shown in Fig. 4. Between 300–1200 K, both Li and O ions exhibit single vibration peaks, confirming ion localization and minimal diffusion. It is consistent with the normal state in Figs. 3(a) and 3(b). At 1300 K, O ions retain a single vibration peak, while Li ions display an additional broad peak at  $\sim 2.3$  Å. This signals a transition in Li ion: Li sublattice melting and the onset of superionic behavior corresponding to Fig. 3(c). At 1800 K, complete melting [Fig. 3(d)] erases these features. Together, these results confirm the superionic transition occurs near 1300 K, with the elastic softening in Fig. 2 directly linked to enhanced Li-ion mobility.

Our results reproduce the  $C_{11}$  softening behavior reported by He [22] and Gupta [20], who observed similar trends at specific temperatures. However, the inflection in  $C_{11}$  here arises from the accelerated Li ion diffusion rather than a superionic transition. As evidenced by the constant activation energy in Fig. 1(b) and the absence of a board peak in Fig. 4(a), the softening regime (1100–1200 K) remains within the normal state. The superionic transition occurs at a higher temperature, distinct from the intermediate softening state.

### C. Transition mechanism

The thermally induced intrinsic defect Frenkel pair is widely considered the primary mechanism for superionic transition in fluorite and antifluorite materials at elevated temperatures [21,24,25,55–57]. A Frenkel pair can be generated as follows:

$$A_A^{\times} = A_i^{\bullet} + V'_A.$$

The defect reaction is expressed using Kröger-Vink notation, taking a monovalent ion as an example. Here, A represents an atom, i denotes an interstitial site, and V represents a vacancy. The combination of an interstitial site and a vacancy forms a Frenkel pair. Schematic of a Frenkel pair in  $\text{Li}_2\text{O}$  shows a Li-ion move from a tetrahedral site to an octahedral interstitial, creating a vacancy at its original position [Fig. 5(b)].

According to the definition of Frenkel defects, the population of octahedral interstitial Li ions ( $\text{Li}_{\text{Oct}}$ ), serves as a direct measure of Frenkel pair concentration and a key indicator of defect-mediated ion transport. As shown in Fig. 6,  $\text{Li}_{\text{Oct}}$

is nearly absent between 300–900 K, consistent with limited Li-ion diffusion. Above 1100 K, its population rises sharply, signaling increased Frenkel pair formation and the onset of structural disorder.

To further evaluate its role, we analyzed the residence time of Li ions at different sites (Table I, Fig. S10 [46]). Figure 5 shows the possible diffusion paths, Figs. 5(a) and 5(b) show diffusion via  $\text{Li}_{\text{Oct}}$  and tetrahedral Li ions ( $\text{Li}_{\text{Tet}}$ ), while Figs. 5(c) and 5(d) show diffusion only via  $\text{Li}_{\text{Tet}}$ . Even at low temperatures, over 85% of  $\text{Li}_{\text{Oct}}$  diffuse within 1 ps, and increase to nearly 100% above 1200 K. Below 1300 K,  $\text{Li}_{\text{Tet}}$  present less than 30% diffusion events within 1 ps. Above 1300 K, its contribution to superionic state becomes considerable (~37%). It's worth noting that across all temperatures,  $\text{Li}_{\text{Oct}}$  displayed markedly higher mobility than  $\text{Li}_{\text{Tet}}$ . These findings underscore a dual mechanism rooted in Frenkel defect dynamics.  $\text{Li}_{\text{Oct}}$ , which shows high dynamical activity, confirms a primary role in fast ion transport and its contribution to the superionic transition.  $\text{Li}_{\text{Tet}}$ , which shows less mobility than  $\text{Li}_{\text{Oct}}$ , also contributes to the superionic transition above 1300 K. Our results differ from Mulliner *et al.* [55], who reported increasing  $\text{Li}_{\text{Oct}}$  residence times with temperature. Instead, we find  $\text{Li}_{\text{Oct}}$  lifetimes remain short and become even shorter at higher temperatures, indicating they act as highly mobile carriers rather than trapped defects. Compared with the results reported by Mulliner *et al.*, the present study adopts a different computational approach. An empirical potential was employed by Mulliner, whose accuracy in capturing defect and diffusion behavior may be limited. For instance, their simulations indicated an increase in the residence time of intersti-

TABLE I. Percentage of Li ions with residence times shorter than 1 ps at octahedral and tetrahedral sites.

Temperature (K)	$\text{Li}_{\text{Oct}}$	$\text{Li}_{\text{Tet}}$
900	89.4	7.5
1000	94.9	11.2
1100	97.6	12.6
1200	99.3	21.1
1300	99.9	37.1
1350	99.9	45.5
1400	100	56.6
1500	100	73.4

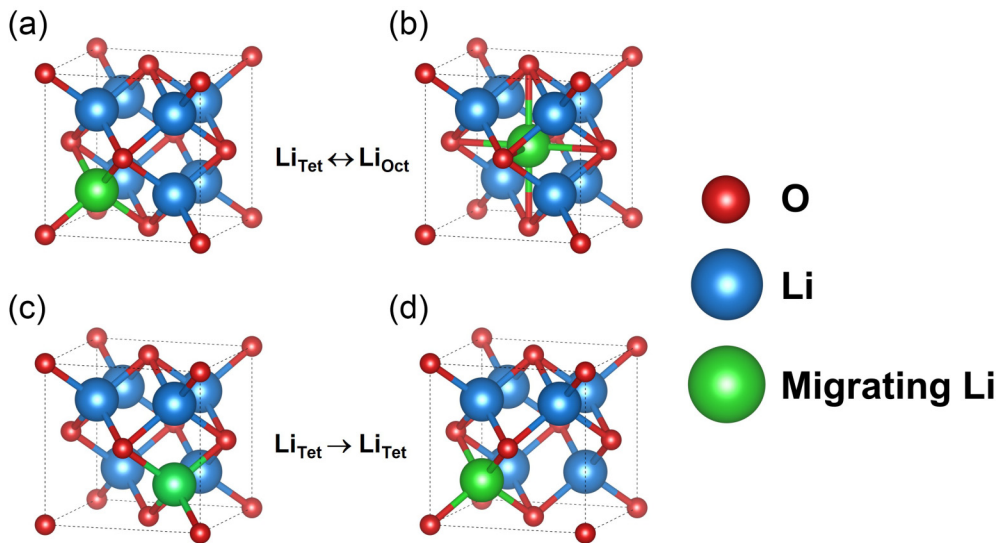


FIG. 5. Schematic illustration of Li<sub>2</sub>O and migration paths. (a) perfect crystal. (b) Crystal containing a thermally generated Frenkel pair. Red balls and blue balls denote O ions and Li ions, respectively. In (a) and (b), Li ions migrate via Oct-Tet transitions, whereas in (c) and (d), Li ions migrate between Tet sites.

tial Li ions with rising temperature, which appears counterintuitive for thermally activated diffusion processes. In contrast, the deep potential model used in this work, trained directly on DFT data, is suitable to capture the energy landscape associated with defect formation and Li-ion migration in Li<sub>2</sub>O. This enables a more accurate characterization of the temperature dependent diffusion mechanisms and offers a more reliable microscopic interpretation of the observed behavior. In particular, the above insights suggest that strategies to increase Li<sub>Oct</sub> population, such as doping, could enhance Li-ion mobility and lower the superionic transition temperature.

#### IV. CONCLUSIONS

Employing a deep potential molecular dynamics (DPMD) framework trained with *ab initio* precision, we investigate the dynamical behavior of lithium oxide. Our DPMD simulations identify three well-defined regimes: a normal crystalline phase (<1300 K); a superionic phase (1300–1700 K) exhibiting gradual type II transition characteristics; and a liquid phase (>1700 K). An obvious softening of elas-

tic constants  $C_{11}$  in 1100–1200 K acts as an acceleration of Li-ion diffusion, which is still classified as normal state. This is also proved by dynamics trajectories and van Hove correlation functions at specific temperatures, which also confirm that it's the melting of Li sublattice that leads to the superionic transition. The superionic transition is governed by the formation of Frenkel pairs, where Li ions move from their original tetrahedral sites to interstitial octahedral sites. A unique defect-mediated diffusion is observed, characterized by fast and effective Li<sub>Oct</sub> diffusion, and much slower Li<sub>Tet</sub> diffusion. This work provides fundamental insights into the structure-property relationship of Li<sub>2</sub>O, linking microscopic ion dynamics to macroscopic properties such as ionic coefficient and elastic constants, and elucidates the microscopic mechanism underlying the superionic transition.

Particularly, these findings can be extended to other materials with fluorite and antifluorite structures, offering a broader framework for investigating ionic diffusion and superionic transitions, and facilitating their practical applications.

#### ACKNOWLEDGMENTS

This research was supported by National Natural Science Foundation of China under Grant No. 11874307. Shaorong Fang and Tianfu Wu from Information and Network Center of Xiamen University are acknowledged for their help with the Graphics Processing Unit (GPU) computing.

The authors declare no competing interests.

#### DATA AVAILABILITY

The data that support the findings of this article are not publicly available upon publication because it is not technically feasible and/or the cost of preparing, depositing, and hosting the data would be prohibitive within the terms of this research project. The data are available from the authors upon reasonable request.

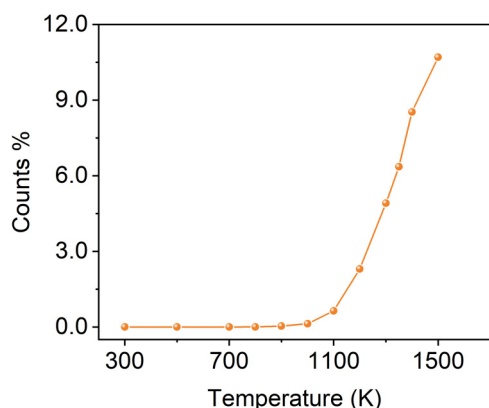


FIG. 6. The number of Li at octahedral interstitial sites.

- [1] Y. Qiao, H. Yang, Z. Chang, H. Deng, X. Li, and H. Zhou, A high-energy-density and long-life initial-anode-free lithium battery enabled by a  $\text{Li}_2\text{O}$  sacrificial agent, *Nat. Energy* **6**, 653 (2021).
- [2] J. H. Strange, S. M. Rageb, A. V. Chadwick, K. W. Flack, and J. H. Harding, Conductivity and NMR study of ionic mobility in lithium oxide, *Faraday Trans.* **86**, 1239 (1990).
- [3] C. E. Johnson and G. W. Hollenberg, Recent advances in the development of solid breeder blanket materials, *J. Nucl. Mater.* **123**, 871 (1984).
- [4] F. Devynck, M. Iannuzzi, and M. Krack, Frenkel pair recombinations in  $\text{UO}_2$ : Importance of explicit description of polarizability in core-shell molecular dynamics simulations, *Phys. Rev. B* **85**, 184103 (2012).
- [5] P. C. M. Fossati, P. A. Burr, M. W. D. Cooper, C. O. T. Galvin, and R. W. Grimes, Superionic transition in uranium dioxide: Insights from molecular dynamics and lattice dynamics simulations, *Phys. Rev. Mater.* **8**, 115404 (2024).
- [6] S. P. Jand, Q. Zhang, and P. Kaghazchi, Theoretical study of superionic phase transition in  $\text{Li}_2\text{S}$ , *Sci. Rep.* **7**, 5873 (2017).
- [7] J. R. Nelson, R. J. Needs, and C. J. Pickard, High-pressure  $\text{CaF}_2$  revisited: A new high-temperature phase and the role of phonons in the search for superionic conductivity, *Phys. Rev. B* **98**, 224105 (2018).
- [8] J. B. Boyce and B. A. Huberman, Superionic conductors: Transitions, structures, dynamics, *Phys. Rep.* **51**, 189 (1979).
- [9] D. A. Keen, S. Hull, A. C. Barnes, P. Berastegui, W. A. Crichton, P. A. Madden, M. G. Tucker, and M. Wilson, Nature of the superionic transition in  $\text{Ag}^+$  and  $\text{Cu}^+$  halides, *Phys. Rev. B* **68**, 014117 (2003).
- [10] A. J. E. Rettie *et al.*, A two-dimensional type I superionic conductor, *Nat. Mater.* **20**, 1683 (2021).
- [11] G. Krenzer, J. Klarbring, K. Tolborg, H. Rossignol, A. R. McCluskey, B. J. Morgan, and A. Walsh, Nature of the superionic phase transition of lithium nitride from machine learning force fields, *Chem. Mater.* **35**, 6133 (2023).
- [12] Z. Liu, P.-H. Chien, S. Wang, S. Song, M. Lu, S. Chen, S. Xia, J. Liu, Y. Mo, and H. Chen, Tuning collective anion motion enables superionic conductivity in solid-state halide electrolytes, *Nat. Chem.* **16**, 1584 (2024).
- [13] J.-A. Hernandez and R. Caracas, Superionic-superionic phase transitions in body-centered cubic  $\text{H}_2\text{O}$  ice, *Phys. Rev. Lett.* **117**, 135503 (2016).
- [14] J. Liang *et al.*, Site-occupation-tuned superionic  $\text{Li}_x\text{ScCl}_{3+x}$  halide solid electrolytes for all-solid-state batteries, *J. Am. Chem. Soc.* **142**, 7012 (2020).
- [15] Y. Kato, S. Hori, T. Saito, K. Suzuki, M. Hirayama, A. Mitsui, M. Yonemura, H. Iba, and R. Kanno, High-power all-solid-state batteries using sulfide superionic conductors, *Nat. Energy* **1**, 16030 (2016).
- [16] C. Yu *et al.*, Superionic conductivity in lithium argyrodite solid-state electrolyte by controlled Cl-doping, *Nano Energy* **69**, 104396 (2020).
- [17] M. Silllassen, P. Eklund, N. Pryds, E. Johnson, U. Helmersson, and J. Böttiger, Low-temperature superionic conductivity in strained yttria-stabilized zirconia, *Adv. Funct. Mater.* **20**, 2071 (2010).
- [18] Y. Meng, M. Akbar, J. Gao, M. Singh, T.-W. Chiu, B. Wang, C. Xia, and L. Fan, Superionic conduction of self-assembled heterostructural  $\text{LSCrF-CeO}_2$  electrolyte for solid oxide fuel cell at 375–550 °C, *Appl. Surf. Sci.* **645**, 158832 (2024).
- [19] M. K. Gupta, B. Singh, P. Goel, R. Mittal, S. Rols, and S. L. Chaplot, Lithium diffusion in  $\text{Li}_2\text{X}$  ( $\text{X} = \text{O}, \text{S}$ , and  $\text{Se}$ ): *Ab initio* simulations and inelastic neutron scattering measurements, *Phys. Rev. B* **99**, 224304 (2019).
- [20] M. K. Gupta, P. Goel, R. Mittal, N. Choudhury, and S. L. Chaplot, Phonon instability and mechanism of superionic conduction in  $\text{Li}_2\text{O}$ , *Phys. Rev. B* **85**, 184304 (2012).
- [21] M. Hayoun, M. Meyer, and A. Denieport, Complex atomic-diffusion mechanism in ionic superconductors: The case of the lithium-oxide antifluorite, *Acta Mater.* **53**, 2867 (2005).
- [22] Y. He, S. Sun, and H. Li, *Ab initio* molecular dynamics investigation of the elastic properties of superionic  $\text{Li}_2\text{O}$  under high temperature and pressure, *Phys. Rev. B* **103**, 174105 (2021).
- [23] P. Goel, N. Choudhury, and S. L. Chaplot, Superionic behavior of lithium oxide  $\text{Li}_2\text{O}$ : A lattice dynamics and molecular dynamics study, *Phys. Rev. B* **70**, 174307 (2004).
- [24] T. Oda and S. Tanaka, Modeling of Li diffusivity in  $\text{Li}_2\text{O}$  by molecular dynamics simulation, *J. Nucl. Mater.* **386**, 1087 (2009).
- [25] A. Jaberi, J. Song, and R. Gauvin, Study of lithium transport in  $\text{Li}_2\text{O}$  component of the solid electrolyte interphase in lithium-ion batteries, *Comput. Mater. Sci.* **237**, 112914 (2024).
- [26] K. Suzuki, K. Ritchie, E. Kajikawa, T. Fujiwara, and A. Kusumi, Rapid hop diffusion of a G-protein-coupled receptor in the plasma membrane as revealed by single-molecule techniques, *Biophys. J.* **88**, 3659 (2005).
- [27] I.-C. Yeh and G. Hummer, Diffusion and electrophoretic mobility of single-stranded RNA from molecular dynamics simulations, *Biophys. J.* **86**, 681 (2004).
- [28] T. Paul, N. Vadakkayil, and S. K. Das, Finite-size scaling in kinetics of phase separation in certain models of aligning active particles, *Phys. Rev. E* **109**, 064607 (2024).
- [29] D. Liu, B. Wang, Y. Wu, A. S. Vasenko, and O. V. Prezhdo, Breaking the size limitation of nonadiabatic molecular dynamics in condensed matter systems with local descriptor machine learning, *Proc. Natl. Acad. Sci. USA* **121**, e2403497121 (2024).
- [30] O. T. Unke *et al.*, Biomolecular dynamics with machine-learned quantum-mechanical force fields trained on diverse chemical fragments, *Sci. Adv.* **10**, eadn4397 (2024).
- [31] P. Zhang, C. Chen, M. Feng, C. Sun, and X. Xu, Hydroxide and hydronium ions modulate the dynamic evolution of nitrogen nanobubbles in water, *J. Am. Chem. Soc.* **146**, 19537 (2024).
- [32] J. Yang and S. Liu, Topological phase transitions in perovskite superlattices driven by temperature, electric field, and doping, *Phys. Rev. B* **110**, 214112 (2024).
- [33] R. Bian *et al.*, Developing fatigue-resistant ferroelectrics using interlayer sliding switching, *Science* **385**, 57 (2024).
- [34] S. Wang, Y. Liu, and Y. Mo, Frustration in super-ionic conductors unraveled by the density of atomistic states, *Angew. Chem. Int. Ed.* **62**, e202215544 (2023).
- [35] M. De La Puente, R. David, A. Gomez, and D. Laage, Acids at the edge: Why nitric and formic acid dissociations at air–water interfaces depend on depth and on interface specific area, *J. Am. Chem. Soc.* **144**, 10524 (2022).
- [36] L. Zhang, J. Han, H. Wang, R. Car, and E. W., Deep potential molecular dynamics: A scalable model with the accuracy of quantum mechanics, *Phys. Rev. Lett.* **120**, 143001 (2018).

- [37] S. Yang, J. Chen, C.-F. Liu, and M. Chen, Evolution of flat bands in MoSe<sub>2</sub>/WSe<sub>2</sub> moiré lattices: A study combining machine learning and band unfolding methods, *Phys. Rev. B* **110**, 235410 (2024).
- [38] H. Wang, L. Zhang, J. Han, and E. Weinan, DeePMD-kit: A deep learning package for many-body potential energy representation and molecular dynamics, *Comput. Phys. Commun.* **228**, 178 (2018).
- [39] G. Kresse and D. Joubert, From ultrasoft pseudopotentials to the projector augmented-wave method, *Phys. Rev. B* **59**, 1758 (1999).
- [40] G. Kresse and J. Furthmüller, Efficient iterative schemes for *ab initio* total-energy calculations using a plane-wave basis set, *Phys. Rev. B* **54**, 11169 (1996).
- [41] P. E. Blöchl, Projector augmented-wave method, *Phys. Rev. B* **50**, 17953 (1994).
- [42] J. P. Perdew, K. Burke, and M. Ernzerhof, Generalized gradient approximation made simple, *Phys. Rev. Lett.* **77**, 3865 (1996).
- [43] D. P. Kingma and J. Ba, Adam: A method for stochastic optimization, [arXiv:1412.6980](https://arxiv.org/abs/1412.6980).
- [44] Y. You, D. Zhang, F. Wu, X. Cao, Y. Sun, Z.-Z. Zhu, and S. Wu, Principal component analysis enables the design of deep learning potential precisely capturing LLZO phase transitions, *npj Comput. Mater.* **10**, 57 (2024).
- [45] D. Zhang, Y. You, F. Wu, X. Cao, T.-Y. Lü, Y. Sun, Z.-Z. Zhu, and S. Wu, Exploring the relationship between composition and Li-ion conductivity in the amorphous Li-La-Zr-O system, *ACS Materials Lett.* **6**, 1849 (2024).
- [46] See Supplemental Material at <http://link.aps.org/supplemental/10.1103/4z6n-zfdr> for details of training dataset, calculation details, reliability of the deep potential function, and figures referenced in the main text, which contains Refs. [58,59].
- [47] J. Ryu, T. Oda, and H. Tanigawa, Comparison and validation of the lattice thermal conductivity formulas used in equilibrium molecular dynamics simulations for binary systems, *Comput. Mater. Sci.* **178**, 109615 (2020).
- [48] A. Annamareddy and J. Eapen, Low dimensional string-like relaxation underpins superionic conduction in fluorites and related structures, *Sci. Rep.* **7**, 44149 (2017).
- [49] Y. Oishi, Y. Kamei, M. Akiyama, and T. Yanagi, Self-diffusion coefficient of lithium in lithium oxide, *J. Nucl. Mater.* **87**, 341 (1979).
- [50] S. Lorger, R. Usiskin, and J. Maier, Transport and charge carrier chemistry in lithium oxide, *J. Electrochem. Soc.* **166**, A2215 (2019).
- [51] Y. C. Chen, C. Y. Ouyang, L. J. Song, and Z. L. Sun, Electrical and lithium ion dynamics in three main components of solid electrolyte interphase from density functional theory study, *J. Phys. Chem. C* **115**, 7044 (2011).
- [52] M. M. Islam and T. Bredow, Density functional theory study for the stability and ionic conductivity of Li<sub>2</sub>O surfaces, *J. Phys. Chem. C* **113**, 672 (2009).
- [53] X.-F. Li, X.-R. Chen, C.-M. Meng, and G.-F. Ji, Ab initio calculations of elastic constants and thermodynamic properties of Li<sub>2</sub>O for high temperatures and pressures, *Solid State Commun.* **139**, 197 (2006).
- [54] S. Hull, T. W. D. Farley, W. Hayes, and M. T. Hutchings, The elastic properties of lithium oxide and their variation with temperature, *J. Nucl. Mater.* **160**, 125 (1988).
- [55] A. D. Mulliner, P. C. Aeberhard, P. D. Battle, W. I. F. David, and K. Refson, Diffusion in Li<sub>2</sub>O studied by non-equilibrium molecular dynamics for 873 < T/K < 1603, *Phys. Chem. Chem. Phys.* **17**, 21470 (2015).
- [56] T. W. D. Farley, W. Hayes, S. Hull, M. T. Hutchings, and M. Vrtis, Investigation of thermally induced Li<sup>+</sup> ion disorder in Li<sub>2</sub>O using neutron diffraction, *J. Phys.: Condens. Matter* **3**, 4761 (1991).
- [57] M. Hayoun, Migration and correlation in highly defective systems: Fast-diffusion in lithium oxide, *Acta Mater.* **56**, 1366 (2008).
- [58] G. Clavier, N. Desbiens, E. Bourasseau, V. Lachet, N. Brusselle-Dupend, and B. Rousseau, Computation of elastic constants of solids using molecular simulation: Comparison of constant volume and constant pressure ensemble methods, *Mol. Simul.* **43**, 1413 (2017).
- [59] Y. Y. Liu, M. C. Billone, A. K. Fischer, S. W. Tam, R. G. Clemmer, and G. W. Hollenberg, Solid tritium breeder materials-Li<sub>2</sub>O and LiAlO<sub>2</sub>: A data base review, *Fusion Technol.* **8**, 1970 (1985).